Acta Materialia 263 (2024) 119499

Contents lists available at ScienceDirect

Acta Materialia

journal homepage: www.elsevier.com/locate/actamat

Full length article

# Unveiling the radiation-induced defect production and damage evolution in tungsten using multi-energy Rutherford backscattering spectroscopy in channeling configuration

S. Markelj [a,*], X. Jin [b], F. Djurabekova [b], J. Zavašnik [a], E. Punzón-Quijorna [a], T. Schwarz- Selinger [c], M.L. Crespillo [d], G. García López [d], F. Granberg [b], E. Lu [b], K. Nordlund [b], A. Šestan [a], M. Kelemen [a]

[a] Jožef Stefan Institute, Jamova cesta 39, 1000 Ljubljana, Slovenia
[b] Department of Physics, University of Helsinki, Helsinki, Finland
[c] Max-Planck-Institut für Plasmaphysik (IPP), Garching, Germany
[d] Center for Micro Analysis of Materials (CMAM), Universidad Autónoma de Madrid (UAM), Cantoblanco, 28049-Madrid, Spain

ARTICLE INFO

*Keywords:*
Tungsten
Defects
C-RBS
Displacement damage
Molecular dynamic simulations
TEM

ABSTRACT

Radiation-induced defect production in tungsten was studied by a combination of experimental and simulation methods. The analysis of structural defects was performed using multi-energy Rutherford backscattering spectroscopy in channeling configuration (multi-energy C-RBS). To create different microstructures, (111) tungsten (W) single crystals were irradiated with W ions at two different doses (0.02 and 0.2 dpa) at 290 K. Detailed transmission electron microscopy (TEM) analysis of the samples revealed the presence of dislocation lines and loops of different sizes. The RBSADEC code was used to simulate the measured C-RBS spectra, recorded with four different He beam energies along the ⟨111⟩ direction. For the first time for tungsten, molecular dynamics (MD) simulations of overlapping cascades were used as input. The well-known method of randomly displaced atoms (RDA) was applied for comparison. RDA does not provide a satisfactory understanding of the nature of the induced defect structure. With MD, a very good agreement between the simulated and experimental spectra was obtained for the sample prepared at a lower dose, despite the fact that the absolute defect densities are two orders of magnitude higher than those found with TEM. A discrepancy is observed for the high-dose-irradiated sample, which is ascribed to the presence of extended defects such as dislocation lines, which are clearly observed by TEM, but cannot be formed in finite size MD cells. RBSADEC with MD cells as input can describe correctly the response of the RBS signal with analysing beam energy while RDA as input gives the wrong trend.

## 1. Introduction

Tungsten (W) is one of the main material candidates for the plasma-facing components in future fusion reactors because of its favourable properties such as high melting temperature, high thermal conductivity and low intrinsic hydrogen isotope (HI) retention. However, in a future thermonuclear fusion environment the 14 MeV neutrons from the D-T fusion reaction will create defects in the crystal lattice, altering the material properties. Due to the nature of the displacement damage caused by neutrons, irradiation with high-energy ions (such as MeV W ions) is a good proxy for neutron irradiation [1,2], excluding transmutation, helium production and most importantly activation of the material. Heavy ion and neutron irradiation result in similar structural damage because: neutrons first impact on a W atom (primary knock-on-atom), which is knocked out of its position with a significant energy transfer. This energetic W ion then causes further displacement damage in the material and is, therefore, responsible for most of the displacement damage caused during a neutron impact. In the context of heavy ion or neutron irradiation, displacement damage refers to the displacement of lattice atoms from their equilibrium position in the crystal lattice and the subsequent creation of lattice defects such as vacancies, self-interstitial atoms, vacancy clusters, voids and dislocation lines/loops.

In material science, there are many well-established methods used

* Corresponding author.
*E-mail address:* sabina.markelj@ijs.si (S. Markelj).

https://doi.org/10.1016/j.actamat.2023.119499
Received 21 June 2023; Received in revised form 3 November 2023; Accepted 3 November 2023
Available online 4 November 2023

for characterizing a material structure and its defects [3], such as transmission electron microscopy (TEM) [4] and positron annihilation spectroscopy (PAS) [5]. Although these are powerful techniques commonly used for defect characterization, they only address very specific aspects of material characterization. TEM can only visualize large defects such as dislocation loops and lines or large vacancy clusters (nano voids) and does not work on bulk samples. PAS can characterize small defects such as single vacancies [6], but the sensitivity to the atomic structure and chemical environment details are lost at large defect complexes [7]. There are many articles on the characterization of defects in tungsten at different damage doses and temperatures using the above mentioned methods TEM and PAS, e.g. [8,9], but there are only a few reports on the ion channeling technique. Ion channeling is a well-established method for studying material properties related to its crystal structure, in particular lattice disorder and defects evolution induced by ion irradiation [10–12].

In this work Rutherford Backscattering Spectrometry in channeling configuration (C-RBS) [12,13] is used to study the defects produced by heavy ion irradiation in the bulk of single-crystal tungsten. To quantify the crystal structure disorder, the change in the ion yield of the backscattered ions along a specific crystallographic direction is measured [10]. Applying sophisticated software algorithms (overview in [14]), a depth profile of disorder in the damaged crystal (disorder refers to all types of structural imperfections such as point defects, extended defects, distortions etc.) can be obtained from the C-RBS spectrum. However, interpreting the C-RBS spectra and understanding the underlying atomic structures remains a challenge. A number of methods were developed to extract the depth profile of radiation damage using various iterative procedures, such as Monte Carlo simulations (e.g. [15] and references within [16]). However, none of these methods are able to provide a detailed insight into the actual damage structure. Only recently, a software algorithm called RBSADEC (RBS from Arbitrary DEfected Crystals) was developed, which is able to correlate the C-RBS spectra with complex structures of defects, providing insightful information about the type of defects present in the damaged crystal [14,16]. The structure used for the RBSADEC simulations is generated in independent molecular dynamics (MD) simulations of radiation damage build-up.

The aim of this research is to further develop RBSADEC for the interpretation of the C-RBS measurements in tungsten single crystals. The main motivation of this work is to study the strength of C-RBS in detecting specific defect types and to answer the question whether the method can provide complementary or additional information compared to TEM and PAS data. For this purpose, different microstructures were prepared in the material, each containing a dominant defect type. The so-called multi-energy beam C-RBS analysis method was applied in our study as it is known that each type of ion-irradiation-produced defect has a particular influence on the analyzing He beam depending on the energy (i.e., direct backscattering or enhanced dechanneling of the probing beam) [12,17]. Such an approach will provide more detailed information about the type of defects and their local extent.

## 2. Experiment

### 2.1. Sample preparation

Tungsten (W) single crystal (SC) samples with surface orientation (111) were purchased from Surface Preparation Laboratory B.V. The crystals had a purity of 99,999 % and a surface normal aligned with an accuracy $< 0.4^{\circ}$. The top surface was polished to a roughness Ra $< 30$ nm and shaped into model SPL.EU.19. with a diameter of 12 mm, a thickness of 1.5 mm and a side groove of 1 mm with a 0.6 mm hole for a thermocouple, 3 mm deep. The (111) surface orientation was chosen because it exhibits the "strongest" channelling axis for ions, as was shown in [18]. Initial scanning electron microscopy (SEM) characterization of the as-received samples showed surface distortions, such as surface scratches and grooves, that would have made the planned experiments impossible. Electron channeling patterns revealed a distorted near-surface layer possibly formed due to mechanical polishing. Therefore, an additional chemo mechanical vibration polishing procedure (vibro) had to be established and was proven successful by positron annihilation lifetime spectroscopy (PALS) measurements. Namely, for the additionally vibro-polished samples we obtained a shorter positron lifetime, which decreased from 118 ps to 108 ps, when comparing the as-received and vibro-polished samples, respectively, indicating a better sample quality for the vibro-polished samples. After polishing, the samples were high-temperature annealed by electron beam heating at the Max-Planck-Institut für Plasmaphysik (IPP), Garching: 5 min at 2350 K with a slow cooling ramp. The quality of the final samples was assessed by SEM-based electron channeling contrast imaging (ECCI), which produces a Kikuchi-like pattern strongly dependent on the crystal structure of the single-crystal sample. In ECCI mode, it is possible to detect the presence of dislocations and possible polycrystalline films (which prevent the formation of the pattern). The undisturbed channeling patterns obtained for all samples proved that the samples were single crystals and that no polycrystalline layer had formed on the surface. After successful initial preparation, the samples were ready for the creation of defects by ion irradiation. For this purpose, the cooled sample holder was modified with a 7° tilt and 11° rotation, which was necessary for avoiding undesired channelling orientation during irradiations. The samples were irradiated in the TOF beam line of the tandem accelerator at IPP [19] with 10.8 MeV W ions at 290 K. The irradiation was performed by x- and y-scanning of the W beam for lateral homogeneous implantation. The sample denoted as '78g' was irradiated to a low W fluence of $5.8 \times 10^{16}\, m^{-2}$ with the aim to produce dominantly single vacancies, as Hu et al. [8] showed for these irradiation conditions. In [8] they focused mainly on characterization of vacancy-type defects; however, as shown in [9,20], self-interstitial-type defects such as dislocation loops and lines will be also present. At these irradiation conditions (low dpa), dislocation loops are expected to be dominant in the material [9,20]. As it was not clear from the beginning whether a low-dose irradiated sample would have any effect on the C-RBS signal, a sample with a higher dose was prepared in addition. The sample denoted as '78f' was irradiated with a W fluence of $5.8 \times 10^{17}$ $m^{-2}$ and is referred to as the 'heavily damaged standard'. For such high W fluence/damage dose it was shown in [9] that numerous dislocation lines are formed, replacing dislocation loops as the dominantly visible defect. Using a displacement energy of 90 eV [21] and evaluating the "vacancy.txt" output of the "Ion Distribution and Quick Calculation of Damage" calculation option of the SRIM 2008.04 code [22], a displacement-damaged zone extending down to 1.3 μm was created, with a peak damage of 0.02 displacement per atom (dpa) at a depth of 0.6 μm for sample 78g and 0.2 dpa for sample 78f. Sample 78g was half covered during the W ion irradiation to have a defect-free single crystal for reference. The damage rate for sample 78g (0.02 dpa) was $1.0 \times 10^{-4}$ dpa/s. and for sample 78f (0.2 dpa) $1.2 \times 10^{-4}$ dpa/s. The peak damage rates are two orders of magnitude higher.

### 2.2. Analysis techniques

The C-RBS measurements were performed at the Center for Micro Analysis of Materials (CMAM) of the Universidad Autónoma de Madrid (UAM), Spain, [23] where a 5 MV tandem accelerator is installed. The standard C-RBS set-up is placed in a multipurpose chamber connected to a beam line located at the 30° port of the switching magnet. The experimental chamber has a goniometer (Panmure Instruments) with 3-axes of rotation (azimuthal rotation, poloidal rotation θ and tilt), allowing to position the sample at the proper angle (crystallographic orientation) to perform the channeling measurements. RBS measurements in channeling configuration were carried out with a helium beam with energies of 4.5, 4, 3.5 and 3 MeV. Silicon particle detectors (ORTEC, USA) with an energy resolution of 14–16.5 keV placed in IBM

geometry and positioned at scattering angles of 170 and 150° were used to measure the RBS spectra. The samples were analysed by RBS in channeling orientation along the <111> direction. The procedure for finding the axial channeling orientation consists of performing linear scans ranging from −3° to +3° (step size 0.04°) for θ or tilt angles, keeping the other one fixed, and repeating the process until the crystallographic orientation associated with the minimum backscattered yield is found. In this way, we have identified the values of θ-tilt where the minimum yield is measured. This method avoids unnecessary additional irradiation of the sample. To collect the non-oriented (so-called random) spectrum, 100 spectra were collected for a combination of θ and tilt positions within a circle of a 3° angle around the ⟨111⟩ direction and were added to the dataset.

Electron-transparent thin foils for TEM analyses were prepared by a site-specific focused ion beam lift-out technique (FIB, Nanolab 650i, FEI Inc.) at Jožef Stefan Institute (JSI), Slovenia. The W samples were screwed into a custom Al holder, designed to minimize electron and ion beam interference. The azimuthal orientation of the sample was determined by ECCI. Using this setup, thin lamellae in precise crystallographic orientation exposing the [01-1] plane were successfully produced from two differently processed samples. During thinning, stepwise ion polishing was applied to minimize the ion-induced defects [24]. The final lamellae were mounted on a Cu support grid and analysed in a conventional TEM (C-TEM, JEM-2100, JEOL Inc.) and a scanning transmission electron microscope (STEM, ARM200CF, JEOL Inc.). For qualitative comparison and to establish the same background arising from the surface damage and artefacts induced during the sample preparation process, all of the TEM samples were consequently prepared in the same orientation, following the same thinning and post-processing procedures.

### 2.3. Simulation

To gain insights into the damage structure of the irradiated W samples, the C-RBS experiment was simulated using the RBSADEC code [14,25]. This code allows the generation of C-RBS spectra from atomistic models of materials in which the damage was built up in molecular dynamics (MD) simulations of overlapping collision cascades.

The MD simulations were performed in two steps. In the first step, a number of successive overlapping cascades in the W-cell were simulated using the PARCAS MD code [26–28] to generate a set of simulation cells with the different levels of damage corresponding to different irradiation doses. First, cubic W simulation cells were prepared with a side length of about 20 nm oriented in ⟨111⟩ direction. The simulation cells with the perfect BCC lattice were thermally equilibrated at 300 K. Each collision cascade was initiated by a primary knock-on atom (PKA), which was simulated by randomly selecting a lattice atom from the center of the cell and giving it the energy of 10 keV. The dpa production rate in the MD simulations was $2.45\times10^{6}$ dpa/s. A detailed description of this procedure including the random shift of the cell before inserting a new PKA can be found in previous work [29]. By increasing the number of collision cascades, it is possible to generate the MD cells with the damage levels corresponding to irradiation doses from 0 to almost 0.2 dpa according to the Norgett-Robinson-Torrens (NRT) equation [30].

In the second step of the MD simulations, a sample was prepared for the C-RBS spectra simulations using the RBSADEC code. This was done by selecting from the first step of the MD simulations (the overlapping cascades) the MD cells with the damage corresponding to the gradually increasing irradiation doses. These cells were stuck together along the z-direction and relaxed in an additional MD simulation to ensure that all cells were merged together in the most energetically favourable way, and that the entire cell represented a single continuous structure with the damage profile which can be compared to the experiment. In this way, two different types of the MD cells were obtained, and we will distinguish in the following between the primary cells (p-cells), i.e. the 20 nm MD cells in which the damage was built up in collision cascades, and the merged cells (m-cells), which were formed by stacking the p-cells. In the m-cells, the direction of depth is along the z direction. The total length of the m-cells is 1.5 μm.

The increase in dpa in the p-cells to form the m-cell was assessed from the SRIM calculations using the Kinchin-Pease (KP) method, where the calculation of atomic displacements is based on the NRT equation [30]. Therefore, the total number of overlapping cascades will be greater in samples with higher fluence to achieve a corresponding irradiation dose. The m-cells were then relaxed at 300 K and 0 Pa for 60 ps using the MD code LAMMPS [31,32], followed by a quench to almost 0 K in 10 ps. After relaxation and quench, C-RBS simulated spectra were generated from the m-cells. More information on the merging of MD cells can be found in the supplementary materials.

In all the MD simulations, a Finnis-Sinclair type potential adjusted by Ackland and Thetford [33] with a further modification at a short-range interaction part (AT-ZN) [34] was used. This potential has shown satisfactory results in terms of describing the evolution of radiation defects in W [29].

## 3. Results

### 3.1. TEM analysis

The main features of the tungsten samples were identified by conventional transmission electron microscopy (C-TEM). Selected area electron diffraction (SAED) technique was used to determine the zone axis (ZA) and orientation of the crystal planes, and the two-beam bright-field weak-beam (BF WB) technique was used to analyze the defects. Bright-field scanning transmission electron microscopy (BF-STEM) was used to observe the structural defects in the material and to determine the depth of the affected zone [35].

The BF-STEM technique was first used to observe the defects present in the material and to determine the depth of the affected zone. Fig. 1 shows detailed micrographs for sample 78f (0.2 dpa, 290 K). The line defects can be identified, following low-index crystal planes. Under the bright field two-beam condition (TEM BF WB), the sample was tilted in the direction of Burger vectors g(002) and g(011) to expose the defects such as dislocations. It appears, that the dislocation loops form strings parallel to (11–1) planes, where interatomic distances are much larger than in (11–2), the plane which is actually perpendicular to the surface. BF-STEM low-magnification overview micrographs and high-magnification micrographs for defect identification are shown in Fig. 2 for both samples 78f (0.2 dpa, 290 K) and 78g (0.02 dpa, 290 K). The estimated damage depth from the low magnification overviews corresponds well to the simulated damage depth profile: about 1.1 μm for 78f and 0.7 μm for 78g, marked as red lines in the images. In sample 78f (0.2 dpa, 290 K) a dense network of dislocation lines (DL) (length > 100 nm) is observed, which is already visible in the overview micrographs. The directions of DL coincide with 110 > 111 > 11–2 > 111 crystal planes. For sample 78g (0.02 dpa, 290 K) only very short DL (~ 20–30 nm) in ⟨111⟩ direction are observed, with predominance of U-shaped loops around “black dots” (size ~10 nm).

The dislocation density was estimated from BF-STEM micrographs of the 2 $\mu m^2$ area; using the line intercept method [36] it is for sample 78f 1.93 ($\pm$0.14)$\times10^{14}$ $m^{-2}$ and for sample 78g it is 3.19 ($\pm$0.15)$\times10^{14}$ $m^{-2}$. Since the dislocation density is not uniform throughout the irradiated depth, the 2 $\mu m^2$ area was further segmented into 100 nm thick regions and the dislocation density in each segment was calculated by the line-length method [37] (Fig. 3). The total number of dislocations counted in sample 78f (0.2 dpa, 290 K) is almost twice as low as in 78g, 250 vs. 409. In sample 78f, the average defect length is 100 nm; 15% of them are identified as loops and 85% as lines. Loops comprise 21% of the total length and lines 79%. In sample 78g (0.02 dpa, 290 K), the average defect length is 50 nm; 14% of them are loops, 86% are lines. The number of the lines and loops is similar. The difference suggests larger defects in 78f compared to 78g; among these, the loops are relatively

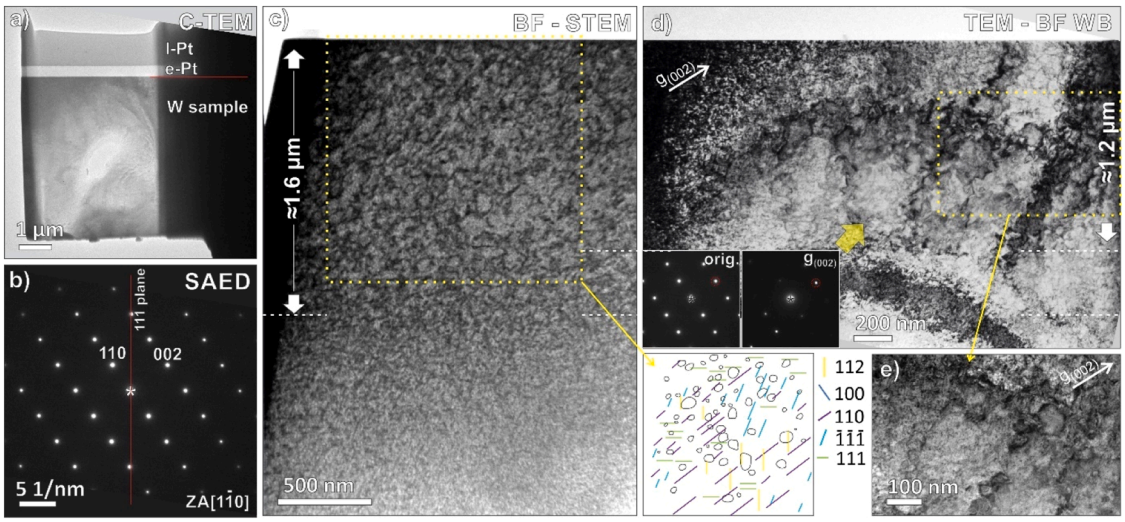


**Fig. 1.** a) C-TEM overview micrograph of the TEM lamella for sample 78f (0.2 dpa, 290 K) with marked main features. b) The SAED pattern, indexed for W and viewed in ZA [1–10]. c) BF-STEM reveals the defects (black lines), observed in the first 1.6 µm below the surface. d) Bright-field weak-beam (TEM-BF WB) micrograph with corresponding SAED with marked two-beam condition for identification of dislocation lines and loops in the sample. e) The marked inset shows the strings of dislocation loops following the {111} planes.

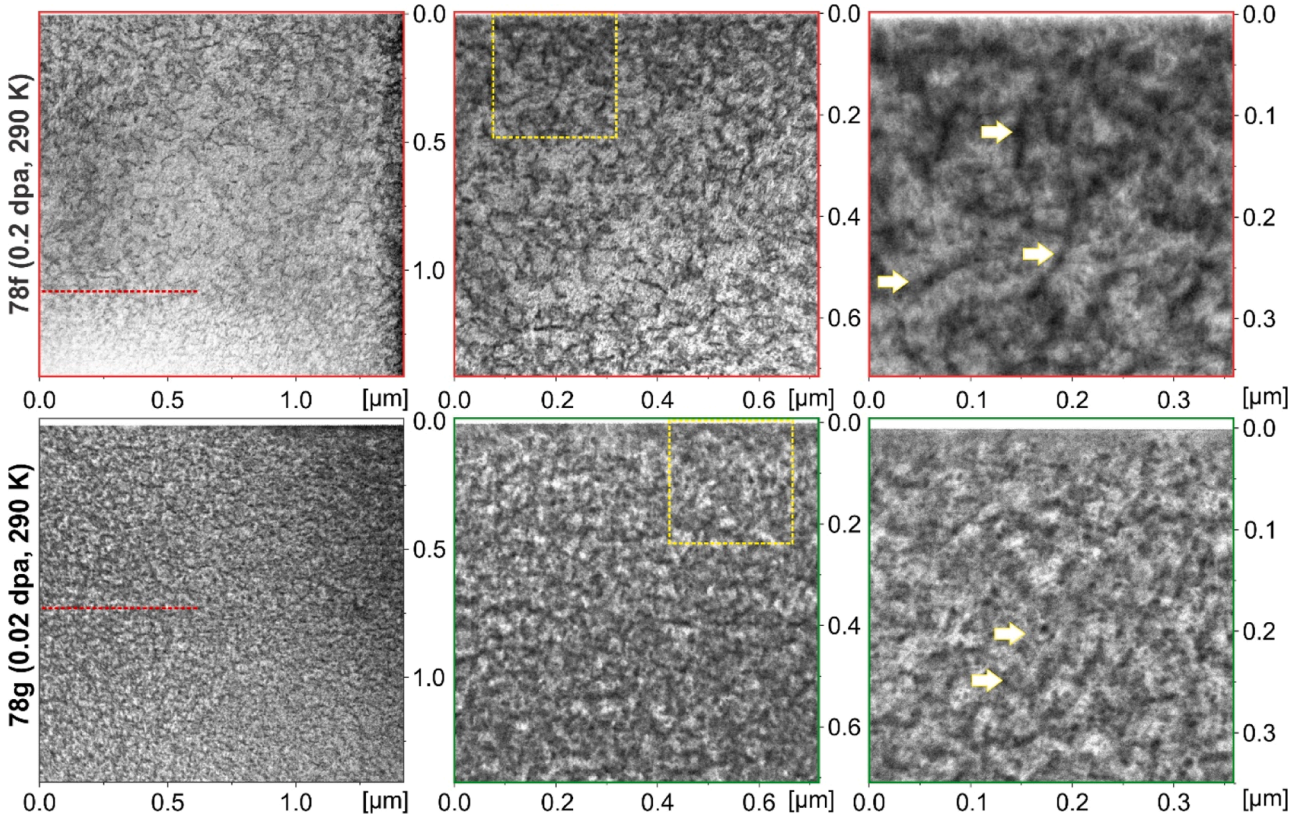


**Fig. 2.** BF-STEM cross-sectional micrographs of sample 78f (red; 0.2 dpa, 290 K) and sample 78g (green; 0.02 dpa, 290 K). The first left most column shows the overview BF-STEM micrographs with marked implantation depth (red dotted line), while the second and the third columns are magnified near-surface regions with defects (marked arrows).

larger in 78f compared to 78g. In sample 78g it can be observed that there are defects also beyond the damaged depth, which we attribute to the Ga ion beam used for lamella thinning. For this reason, we compare our dislocation density with those obtained in [9], where conventional 3 mm disk specimens were prepared by electropolishing, thus avoiding the presence of FIB-induced defects. In [9], the lowest damage dose was 0.05 dpa. Multiplying the volume loop density of $2.1\times10^{22}$ m$^{-3}$ with the loop diameter of $8\times10^{-9}$ m, both given in Fig. 3 in [9], the resulting loop density for 0.05 dpa is $1.68\times10^{14}$m$^{-2}$. No lines were observed at this dose. A similar loop diameter was observed on a W (100) single crystal damaged to a damage dose of 0.04 dpa [20]. At a damage dose of 0.2 dpa, a loop density of $8.4\times10^{13}$ m$^{-2}$ and a line density of $1.5\times10^{14}$ m$^{-2}$ were observed in [9], which together give a dislocation density of $2.3\times10^{14}$ m$^{-2}$. Comparing these dislocation densities with those

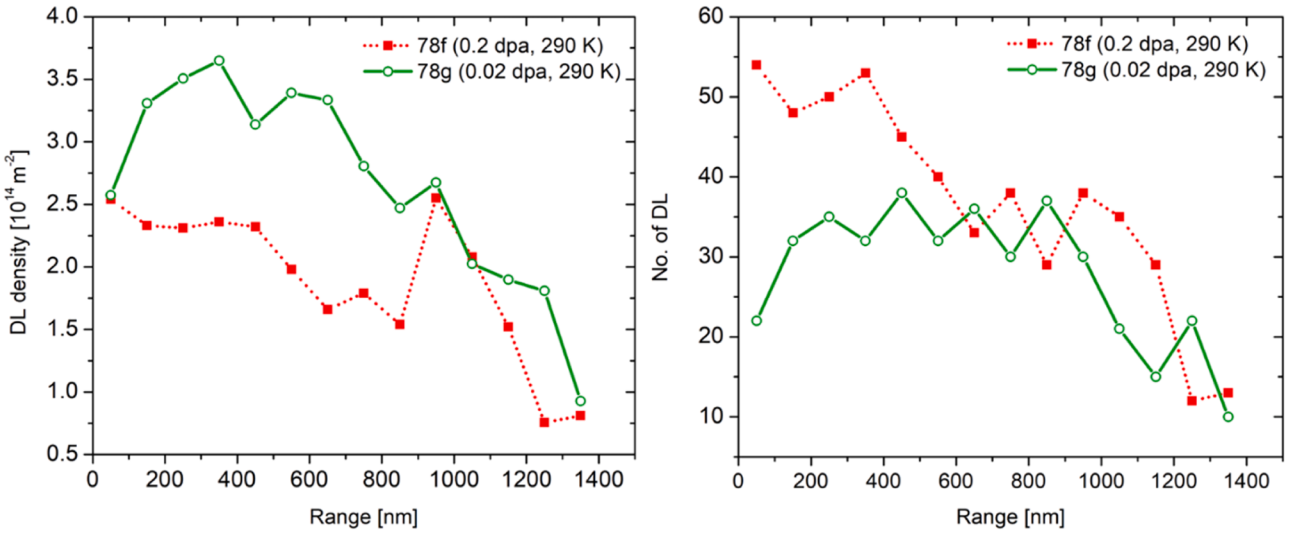


**Fig. 3.** Left: Depth distribution of the dislocation density derived by the line-length method for sample 78f (0.2 dpa, 290 K, red data) and sample 78g (0.02 dpa, 290 K, green data). Right: Depth distribution of the total number of dislocations.

obtained from our study (Fig. 3), we can see that the density is overestimated by a factor of two for our sample 78g with 0.02 dpa. However, the dislocation density obtained in our case for the 0.2 dpa sample is in good agreement with the one from [9]. The TEM sample preparation procedure in [9] avoids FIB-induced damage; however, the sample is prepared parallel to the surface, and only a limited depth can be analyzed. In this case, the TEM sample was thinned at the peak of the SRIM-calculated damage profile.

### 3.2. C-RBS measurements

The RBS measurements were performed in channeling configuration on the samples. As mentioned above, the multi-energy ion beam analysis was used. For this purpose, four He beam energies were used: 4.5, 4.0, 3.5 and 3.0 MeV, impinging the samples along the ⟨111⟩ direction. Spectra of samples 78g (0.02 dpa, 290 K) and 78f (0.2 dpa, 290 K) measured at 4.5 MeV $^4$He energy with the RBS detector at 170° scattering angle are shown in Fig. 4. As mentioned before, sample 78g was

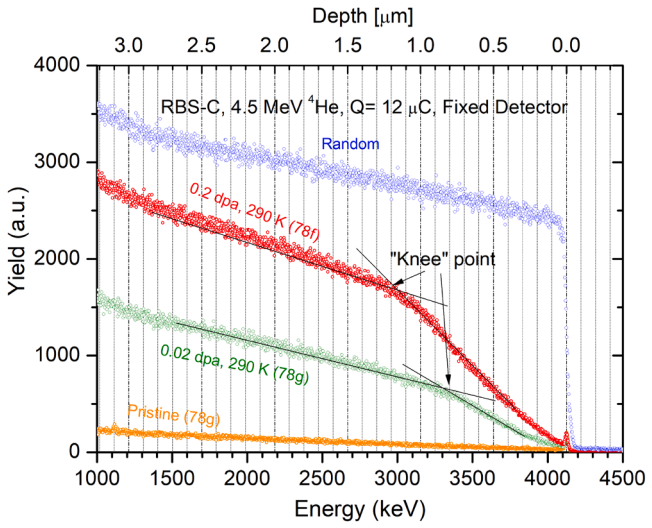


**Fig. 4.** C-RBS spectra in ⟨111⟩ channeling direction obtained at 4.5 MeV at 170° scattering angle. The channeling spectrum obtained on the non-irradiated half of sample is called "Pristine". The "Random", spectrum was obtained by adding 100 spectra collected for a combination of theta, tilt positions around the ⟨111⟩ direction.

half covered during the W-ion irradiation in order to have a defect-free single crystal for reference. RBS spectra were acquired on both sides: on the undamaged side, denoted as Pristine', and on the W-ion irradiated, damaged side (0.02 dpa, 290 K) of the single crystal. Moreover, the undamaged side of the sample was used to obtain also the so-called 'Random' spectrum. All these four spectra are shown in Fig. 4. The spectrum labelled as 'Random' was obtained as described above in the Experiment section. Starting from the aligned ⟨111⟩ orientation, the sample was rotated around with a combination of θ and tilt angles, in the θ range from −3° to 3° and in a tilt range from −3° to 3°. All recorded spectra are then summed into the Random spectrum.

As already mentioned, the yield for the random orientation is the highest compared to the samples oriented in the channeling direction, since it is considered as a non-aligned material with a huge quantity of scattering centers. Such a spectrum is also obtained when a classical RBS spectrum is recorded on a polycrystalline W. However, when the RBS spectrum is recorded in the axial channelling direction ⟨111⟩, the pristine sample exhibits a very low backscattering yield, meaning that the outer most atoms efficiently shadow the more inner atoms of the lattice. For all measured spectra in the channeling direction, a sharp small peak is observed at the highest energy. This is the so-called surface peak, since the surface has a different distribution of atoms than the bulk due to surface reconstruction or surface impurities such as oxides. From the pristine and random spectra, the minimum channeling yield $\chi_{min}$ can be calculated, which is defined as the ratio of the yield of the aligned channel orientation to that of the random orientation at the channel just below the surface peak (~ 20 channels behind) in the spectrum of the pristine crystal [17]. According to spectra shown in Fig. 4, $\chi_{min} \approx 1.3$ %, which means that this sample has a very good crystalline quality [13]. On the other hand, the damaged samples (78f: 0.2 dpa; 78g: 0.02 dpa) exhibit intermediate backscatter yields compared to the other two spectra; it can be seen that the sample that saw the largest dose shows a higher yield, which means that its structure contains a larger concentration of defects (and tends more towards an amorphous material than sample that received a lower dose). It is important to note that the channeling spectra recorded on W-irradiated samples do not show a clear damage peak but are characterized by enhanced dechanneling yield that increases with the analysing yield [17]. Similar behavior was observed also on W damaged to high dose at elevated temperatures [10]. A process called dechanneling occurs when some channeled ions are slightly deflected into a non-channeling direction, behaving as a beam in random direction [38,13]. For this reason, in the case of the damaged samples we can observe that the backscattering yield is only changing its

slope, at an energy of 3.1 MeV for sample 78f and 3.3 MeV for sample 78g, as marked in the figure. There, the slope of the spectrum decreases and approaches that of the spectrum of the pristine W. This is the so-called 'knee point', where the first high energy yield is due to channeled ions backscattering directly from the displaced atoms in the sample and after that the signal is due to dechanneling [38]. The depth scale shown on the top axis is estimated on the basis of the stopping power from SRIM with surface energy approximation [13]. It can be observed that the knee point for the sample 78f is at about 1.2 μm and for the sample 78g it is at 0.8 μm, which is in very good agreement with the observed depth of the defects observed by TEM analysis. We can deduce from the graphs that the RBS-C technique is sensitive to the damage induced by the irradiation, even for the low dose. When the damage in the crystal is increased, the backscattering yield is increased due to the presence of more/larger defects in the crystal. This is observed in the graphs by an increase in the backscattering yield.

When collecting the spectra for "Random", for each point of (θ; tilt), the spectrum for backscattered yield was recorded on pristine sample and the integral of the spectra was calculated in the region of interest just below the surface peak. The integral value is assigned to the orientation (θ; tilt). For the present experiment, this was obtained for 100 (θ; tilt) combinations, resulting in the 3D crown that is shown in Fig. 5a. The minima in the 3D crown show the positions of the planar channels. By connecting the minima one obtains in the cross section the axial ⟨111⟩ channeling direction. Fig. 5b shows the angular scan for θ from −2° to 2° at a fixed tilt angle (0°), where the data present the integral of the backscattered yield on the pristine sample. The integral of the spectra was calculated in the region of interest just below the surface peak. It can be seen that the ⟨111⟩ axial channel is deep and well-defined. The minimum backscattering yield is close to zero in the ⟨111⟩ axial channel orientation showing the high crystalline quality (low defect concentration) of the pristine substrate. The calculated half-angle $\psi_{1/2}$ (pristine) is 0.89°.

### 3.3. Modeling

In order to understand the nature of defects in the irradiated W samples, we compare the C-RBS spectra obtained in the experiments with simulations using the RBSADEC code [14,25] for all four damage levels, i.e. pristine, damaged to 0.2 dpa (78f) and to 0.02 dpa (78g) and fully disordered (Random). The temperature of the simulated targets was set to 290 K. The detection angle and resolution in the simulation were set to be the same as was in the experiment: The detector was at a scattering angle of 170° and had a resolution of 16.5 keV, as was determined from the rise of the RBS edge in the experimental data.

Before comparing the C-RBS spectra from MD simulations of overlapping cascades with the experimental spectra, we used the common approach of randomly displaced atoms (RDA) to estimate the damage profile, which can reproduce the C-RBS spectra measured in the experiments. First, we constructed a new atomistic W cell with a size similar to the m-cells (1.5 μm in z-direction and 19 × 20 $nm^2$ in lateral dimension). The z-direction of the cell is along the ⟨111⟩ axis. In the pristine structure we randomly displaced atoms gradually from the surface to the bulk and compared the simulated C-RBS signal with the experimental one. The atoms were allowed to be randomly displaced in a region with a volume of one-unit cell. When a good agreement between these signals is achieved, the atoms from the next layer (deeper into the bulk) are displaced. Finally, the complete C-RBS spectrum of a simulated structure looks identical to the experimental one and the damage profile expressed in RDAs is obtained. Note that in these simulations, the structure is not relaxed, hence, no information about the nature and the structure of the defects can be deduced.

According to the best fit of the simulated and experimental spectra, shown in Fig. 6, the RDA profiles for the two damaged samples are presented in Fig. 7. There, the RDA profiles are represented by the lines with different colors, while the blue-shaded profile shows the calculated primary damage profile of 10.8 MeV W-ions with a maximum damage

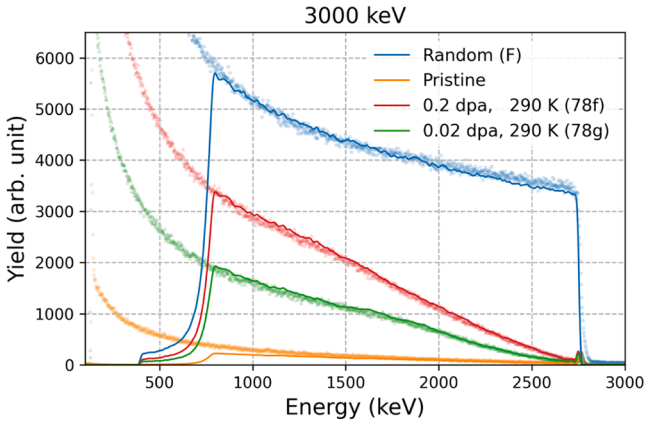


**Fig. 6.** C-RBS experimental and simulated spectra at $^4$He energy of 3 MeV for the two damaged samples together with the ones for the pristine and random. The simulations were performed using randomly displaced atoms and their depth profiles were adjusted to fit the experimental spectra.

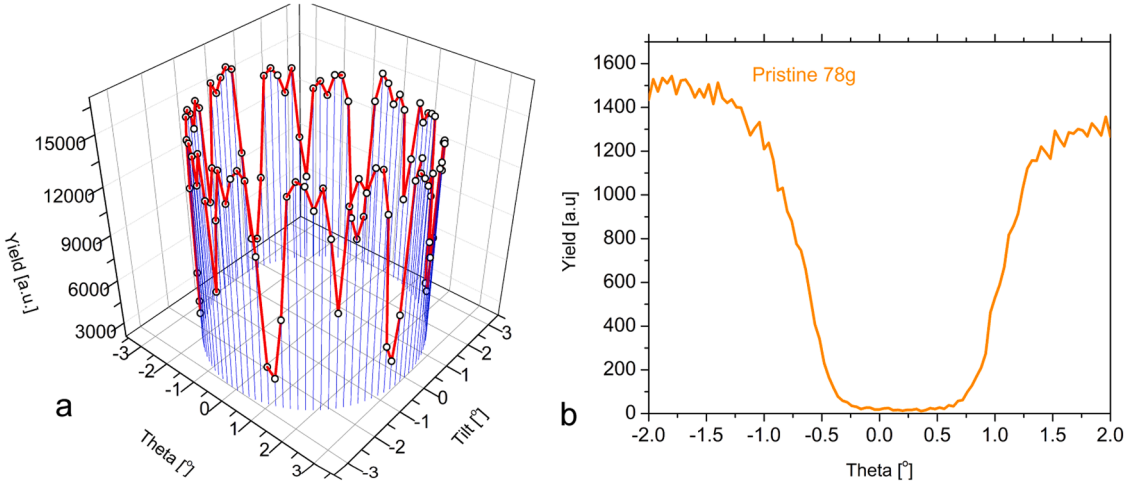


**Fig. 5.** a) 3D backscattering yield plot ("crown") showing the backscatter yield for the pristine half of sample 78g with 3 MeV $^4$He for combinations of θ and tilt. b) Backscattered yield measured as a function of rotation angle θ for 0° tilt at 4.5 MeV $^4$He energy.

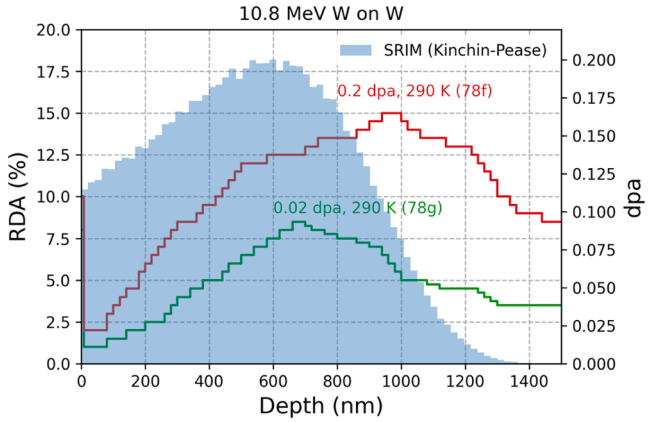


**Fig. 7.** RDA profiles of damaged samples (samples' ID's and the corresponding irradiation conditions are indicated) and the dpa profile of 10.8 MeV W ions on W calculated by SRIM (the blue-shaded area) for which the maximum damage dose is 0.2 dpa.

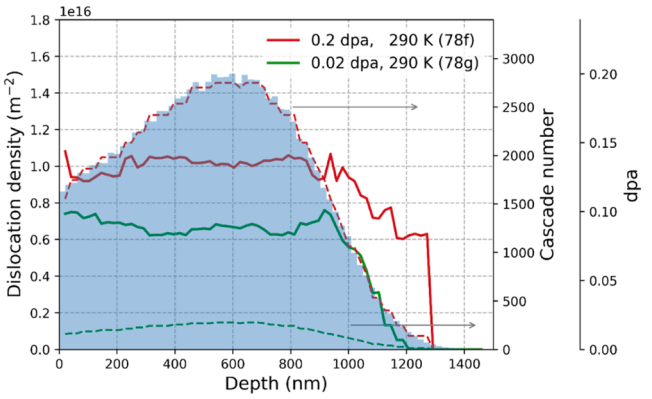


**Fig. 8.** Distributions of dislocation densities in the MD m-cells built to imitate the damage structure corresponding to the samples 78f and 78g, shown by red and green solid lines, respectively. The dashed lines of the corresponding colors show the depth distributions of the number of overlapping cascades simulated to achieve the corresponding irradiation dose. The dpa profile of 10.8 MeV W ions on W calculated by SRIM, for which the maximum damage dose is 0.2 dpa, is represented by the blue-shaded region as in Fig. 7 (arrows pointing to the right y-axis indicate the number of cascades).

dose of 0.2 dpa. The primary damage profile was calculated by SRIM using the 'Quick calculation of Damage' option, with an incident angle of 7° and a threshold displacement energy of 90 eV [39,21]. Comparison of Figs. 6 and 7 leads to the following observations:

i) To fit the surface peaks of the C-RBS spectra generated from the samples 78g and 78f (see Fig. 6), it was necessary to insert RDAs in the surface region, with a rather larger value of approximately 8 % of all atoms in this region, as can be seen in Fig. 7 (sharp peaks in the surface region). However, it should be noted that a similar surface peak is also found in the pristine sample. Thus, it is likely that this small peak indicating surface disorder is not related to the irradiation-induced damage but could originate for example from surface oxide, as already mentioned in section 3.2.
ii) The maximum damage dose produced by W-ion irradiation at 290 K in sample 78f is ten times the maximum dose in sample 78g according to the SRIM calculations (0.2 dpa and 0.02 dpa, respectively). However, the maximum values of RDA required to reproduce the C-RBS spectra of samples 78f and 78g in the bulk region differ only by a factor of 1.8, as shown in Fig. 7 (15 RDA vs. 8.5 RDA, respectively). Moreover, the depths of the peaks of the RDA profiles that were used to fit the experimental C-RBS spectra do not coincide with the depth of the damage peak that was predicted by SRIM, especially for the high dose sample 78f. We also see that the higher the damage dose the deeper the RDA peak is located.
iii) The deeper location of the RDAs compared to SRIM prediction (e.g., beyond 1200 nm) which was necessary to reproduce the C-RBS spectra could be explained by significant dechanneling by larger structural defects. Indeed, large dislocation lines or dislocation loops were observed by TEM. They were formed at shallower depths, but provide strong contribution to the spectra, effectively corresponding to the deeper RDAs.

From the analysis of Figs. 6 and 7 it is clearly concluded that the RDA depth profiles, which are able to reproduce the experimentally measured C-RBS spectra, unfortunately, do not provide a satisfactory understanding of the nature of the induced defect structure in irradiated W samples. Therefore, this lack of agreement motivated us to use the RBSADEC code to simulate the C-RBS spectra from the atomistic models of the W lattice with realistic damage structure produced in collision cascades by means of MD simulations.

Two MD m-cells were prepared according to the recipe previously described in the Section 2.3 for the two W-ion irradiated samples: 78g and 78f, with damage dose of 0.02 dpa and 0.2 dpa, respectively. Fig. 8 shows the depth distribution of the dislocation densities in the MD m-cells for these two samples. The dislocation densities in the MD cells were detected using the dislocation analysis method in OVITO [40]. Dominant dislocation structures in our simulations were identified as ½<111> dislocation loops of interstitial type. For both m-cells, the dislocation densities were basically constant in the first 1 μm region, in which the average densities are around 0.7 $\times 10^{16} m^{-2}$ and 1.0 $\times 10^{16}$ $m^{-2}$ for samples 78g (0.02 dpa) and 78f (0.2 dpa), respectively.

Fig. 9 shows the experimental C-RBS spectra obtained using the He beam of different incident energies (3 - 4.5 MeV) on the <111>-oriented W targets (dots) and the corresponding simulated spectra generated from the MD structures (solid lines). The spectra of the samples 78f and 78g are shown as red and green lines, respectively. The agreement between the simulated and experimental spectra for sample 78g (0.02 dpa, 290 K) is excellent. Some peak-like signals are visible in the C-RBS spectra (for example, the one in the spectrum of sample 78g measured with 4.5 MeV He ions at about 2.7 MeV). These signals are caused by artificial dislocations in the interface between the merged p-cells that were not joined smoothly. Since the total number of peaks is limited and their magnitude is relatively small, this interface effect should not have a significant influence on the simulations, for example by changing the main trend of the C-RBS curve.

It is worth noting that in these simulations the spectra were generated directly from the simulated structures and no fitting was applied. For sample 78f (0.2 dpa, 290 K) the simulated spectra are lower than the experimental ones, showing the lower level of disorder in the simulation cells at this dose compared to the experiment. We also note that in the experiment the "knee" points are more pronounced when a higher $^4$He energy is used, especially, for the sample 78f (0.2 dpa, 290 K). No distinct "knee" points are observed in the simulated spectra. To understand the reason of this difference, a more detailed analysis of the measured C-RBS spectra with increasing He energy is performed. The evaluation of the dependence of the relative disorder level $f_d$ on the energy of the probing ions is conducted using the following expression:

$$f_d = \frac{y_d - y_p}{y_r - y_p}$$

where $y_d$, $y_p$ and $y_r$ are the RBS backscattering yields in the damaged, pristine and random spectra, respectively. The relative disorder levels calculated after the "knee" points at a depth of 1.25 μm for the two damage doses are given in Fig. 10. For the low dose sample 78g (0.02

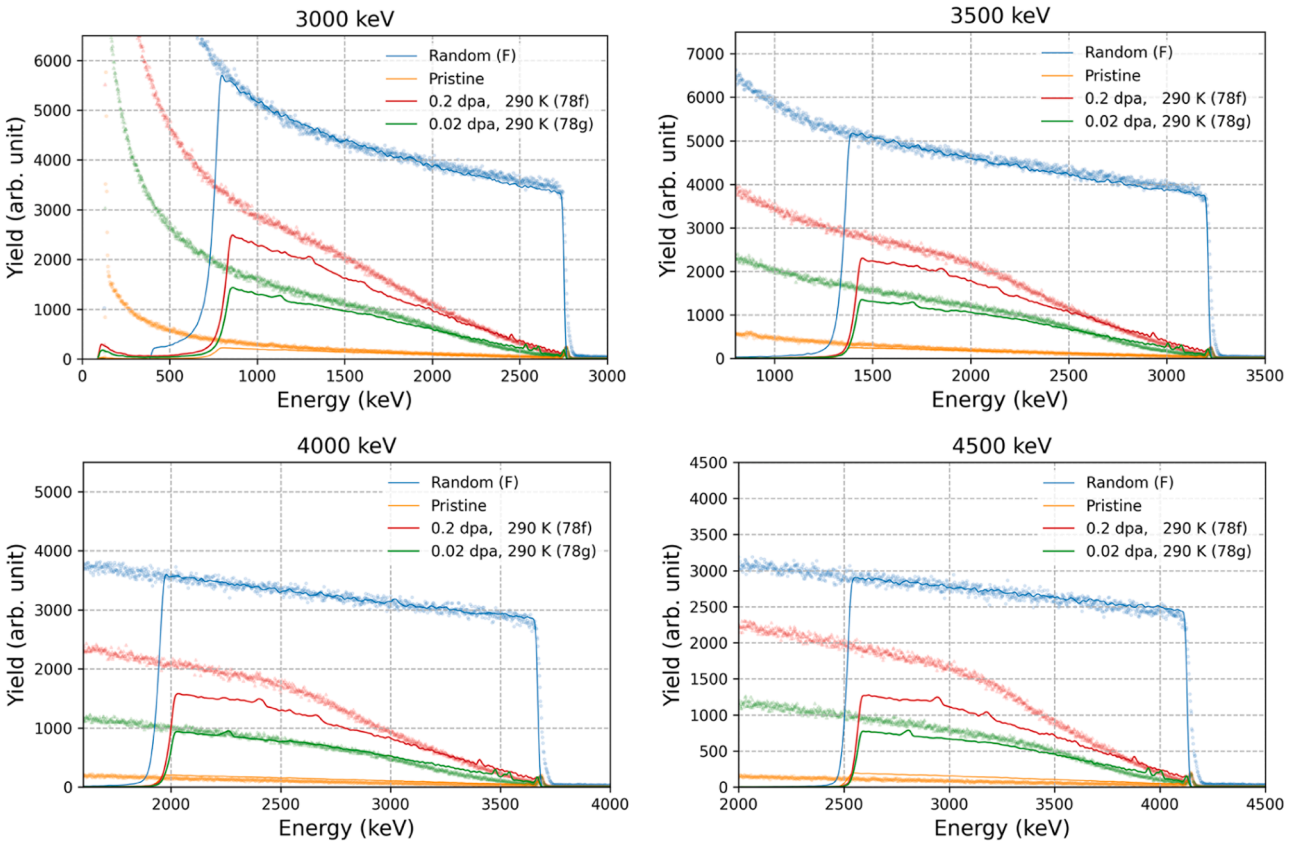


**Fig. 9.** Comparison between the measured C-RBS spectra (dots) and the spectra generated from W-targets containing realistic defects generated using molecular dynamics (lines) for all four measured $^4$He energies.

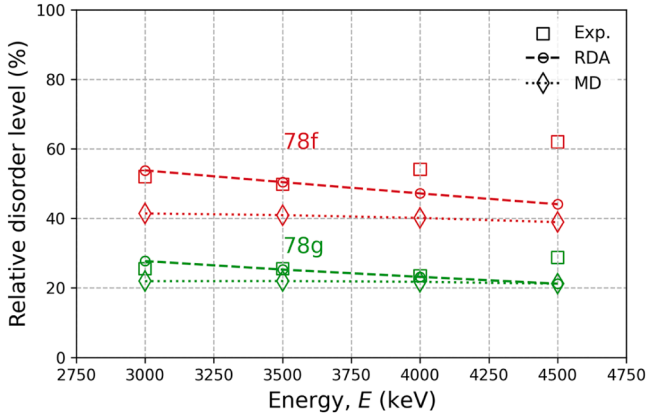


**Fig. 10.** Relative disorder levels as a function of energy calculated from experiments (square), and simulations using the RDA (circle) and MD (rhombus) methods.

dpa at 290 K) a good agreement between the simulated data and experiment is observed. Both show very weak dependence on probing ion energy, which indicates that both experimental and simulated structures developed similar defects, which are predominantly dislocation loops. However, for the high dose sample 78f (0.2 dpa at 290 K) there is a discrepancy in the energy dependence observed for simulated and experimental C-RBS spectra. The relative disorder in the experimental samples increases with increase of the probing ion energy, while it stays constant for the MD cells and even reduces in the RDA-based simulated spectra. Clearly, RDA-type defects do not capture the nature of the defects formed at this dose in W. The discrepancy between experiment and MD m-cells can be explained by the presence of dislocation lines, which are clearly visible in TEM images and have a much larger lateral scale than those grown in the size-limited MD cells. Hence, the analysis of the relative disorder level as a function of ion probing energy can be used to assess the dominant defects in irradiated targets.

## 4. Discussion

Using the RBSADEC code, the C-RBS spectra of displacement-damaged W targets were simulated containing realistic defects generated by MD calculations. A very good agreement between the simulated and experimental C-RBS spectra was obtained for the low dpa sample 78g (0.02 dpa, 290 K) up to 4 MeV, with some discrepancy at 4.5 MeV. Not so good agreement was obtained for the high dpa sample 78f (0.2 dpa, 290 K). As seen in Fig. 2, the TEM analysis of sample 78g showed that at this irradiation dose, the defects produced in collision cascades organized themselves predominantly in dislocation loops, while in the sample 78f under much higher irradiation dose, the dislocation loops are no longer visible and dislocation lines become more dominat. From the TEM analysis, a dislocation density of 3.19 ($\pm$0.15)$\times10^{14}$m$^{-2}$ was obtained for sample 78g and 1.93 ($\pm$0.14)$\times10^{14}$ m$^{-2}$ for sample 78f. The finite size of the MD cells limits the development of the dislocation structure and the simulations of overlapping cascades with both doses resulted in the formation of loops only. The dislocation densities obtained by MD are slightly different for the two samples, namely, about 0.7$\times10^{16}$ m$^{-2}$ for sample 78g and about 1$\times10^{16}$ m$^{-2}$ for sample 78f. Despite the two orders of magnitude difference between the dislocation densities that were obtained in the MD simulations and deduced from the TEM images, the agreement between the simulated and the measured spectra as well as the energy dependence of the disorder level is very good for the low dpa sample 78g.

A plausible explanation for the similarity of the measured and simulated C-RBS spectra despite significant difference on the dislocation

densities could be found by analyzing the size effect of dislocation loops. For this purpose, the C-RBS dechanneling of a [001]-oriented W lattice with only ½<111> dislocation loops of interstitial type in it was calculated. Circular dislocation loops were inserted into the W targets using the BABEL program [41], and then were relaxed by MD using a conjugate gradient algorithm. The same AT-ZN [34] interatomic potential was used in these simulations. In all targets, the total number of inserted interstitial atoms is about the same. Three different loop radii, r, were considered ranging from 3$a$ to 11$a$, where $a = 3.17$ Å is the lattice constant of W. A visualization of dislocation loops after the static relaxation is shown in Fig. 11. More details on the model W targets can be found in the supplementary materials.

After generating C-RBS signals from these new structures using different He ion energies, the dechanneling fractions induced by the dislocation loops were calculated. Fig. 12 shows the dechanneling fractions per dislocation density as a function of He energy. They do not show a strong energy dependence in the high He energy range. However, it is surprising to observe that a larger number of dislocation loops (the left column in Fig. 11) results in a lower dechanneling fraction per dislocation density (blue dots in Fig. 12) than in the structure with larger dislocation loops (the right column in Fig. 11), but with lower density (violet dots in Fig. 12). From this we conclude that as the loop size increases, the dechanneling fraction (per dislocation density) also increases. This can be explained by a dipolar effect [42] which can compensate the lattice distortion with decreaseing loop size. Thus, the dechanneling fraction per dislocation density is expected to increase with the loop size until the dipolar effect is no longer effective. This explains the agreement observed between the spectra generated from

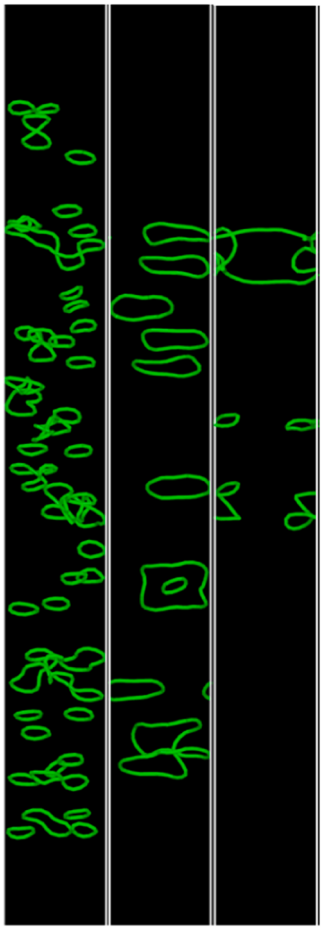

**Fig. 11.** Visualization of model W targets containing ½<111> dislocation loops with different sizes after static relaxation. The initial radii of the loops are 3a (left), 7a (middle) and 11a (right), where a is the lattice constant of W.

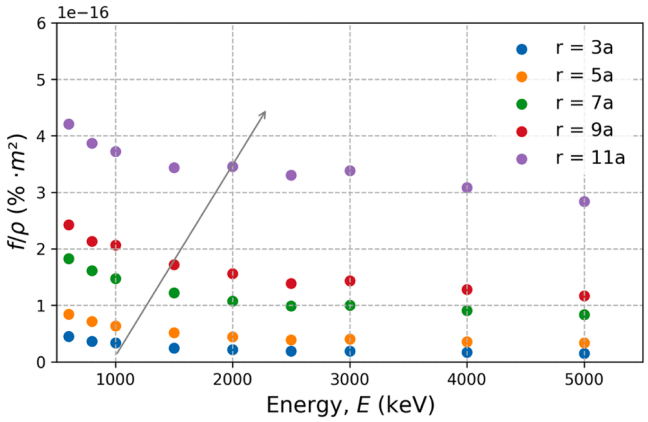


**Fig. 12.** Dechanneling fractions per dislocation density induced by dislocation loops of different sizes as a function of incident He energies. (The arrow indicates the increase of the loop radius, r.).

the MD produced damage with smaller loops but higher density and the experimental ones with much larger loop size but lower density. In [9], a dislocation loop size of about 8 nm in diameter and a loop density of $1.68\times10^{14}$ m$^{-2}$ were observed for a damage dose of 0.05 dpa, giving a radius of 12 $a$. Since those analyses were free from ion-induced defects in the TEM lamella, this gives additional support to the explanation why we obtained good agreement between MD and experiment.

The same explanation does not apply to sample 78f with a much higher dose of 0.2 dpa. In this sample, the TEM analysis shows mainly dislocation lines and no loops. This is a crucial difference, which explains the poorer agreement between the two methods for the samples irradiated at higher dose. Since it is not possible to develop the dislocation loops beyond the simulation box, we cannot conclude whether the dechanneling fraction will continue to increase when the dislocation loops become large enough to become visible as lines in the TEM images. While the limited size of the MD cells does prevent the formation of micrometer-long dislocation networks, this is not a limitation of the simulation by RBSADEC code since the RBS backscattering of individual probing ions occurs from the dislocation core (which is a few Å wide) or from the highly strained atoms in its immediate vicinity (at most a few nanometers from the core). The cell sizes of the MD simulation are much larger than a few nanometers and are hence fully sufficient to describe RBS/channeling also from dislocations. It is worth noticing that the difference between the measured and simulated C-RBS spectra is less dramatic at low $^4$He ion energies. With increase of the $^4$He ion energy the difference is clearly increasing. The enhancement of the dechanneling from the dislocation structures at high energies of probing ions remains to be understood. However, our results clearly indicate that the use of different probing beam energies provides additional and complementary information about the defect structure that is not accessible by single energy C-RBS measurements. At the same time, the C-RBS spectra obtained by using RDA do not provide any additional information and do not follow the trend of the disorder level as a function of energy of the probing beam. With the MD simulation the agreement in the relative disorder level is better but not satisfactory. With such a discrepancy in the dislocation density and the dependence on probing energy, it is clear that the MD simulation needs to be further developed in order to be able to explain the experimental results.

An explanation for the difference between the defect structures observed in the experiment and MD simulations could be the different damage dose rates between the experiment and MD. Indeed, the dose rate in MD simulations is much higher than in the experiments carried out here, due to the limited time- and size-scales reachable. However, previous studies with tungsten have shown that these simulations [29] do show comparable vacancy concentrations to experiments with transient grating spectroscopy [43] and deuterium retention measurements

[44]. For other materials (high entropy alloys), these high dose simulations [16] have yielded good agreement in the dislocation and defect structures observed. In addition, even though the dose rate is higher, the vacancies are immobile on simulation timescales, but practically also on experimental timescales in tungsten. Therefore, vacancies should not be dramatically affected by this discrepancy. On the other hand, interstitials are very mobile, even on simulation timescales, eg. even in the limited time reachable by MD they have time to combine and form clusters, which is also seen. Thus, the effect of the dose rate discrepancy should not be dramatic. The main difference is the size-scales reachable in MD, which do not allow for extensive dislocation networks.

## 5. Conclusion

In this study, C-RBS spectra were measured in ⟨111⟩ axial direction with a $^4$He ion beam at four different energies on two W single crystal samples irradiated with 10.8 MeV W ions at two different doses (78g: 0.02 dpa; 78f: 0.2 dpa) at 290 K and on the undamaged side of sample 78g. In addition, a Random spectrum was measured on the undamaged side of sample 78g, corresponding to a non-aligned single crystal with a large number of scattering centres. For the first time, measured spectra were compared to simulated spectra using the RBSADEC code. For the latter W targets containing realistic defects were generated using MD. A very good agreement is reached between the simulated and the measured spectra for the low dose sample 78g (0.02 dpa, 290 K), where dislocation loops were observed both by TEM analysis and MD simulations with overlapping cascades. In addition, a good agreement was found for the energy dependence of the disorder level for this sample. An explanation was given as to why we still observe a good agreement between the measured and the simulated spectra, despite the difference in the dislocation density between TEM and MD. For the high dose sample 78f (0.2 dpa, 290 K) a discrepancy in the energy dependence was observed for the simulated and experimental C-RBS spectra. The relative disorder in the experiment increases with increase of the probing ion energy, while it stays constant for the simulations with MD cells. In this sample, the TEM analysis reveals mainly dislocation lines, while in the MD simulation we obtain dislocation loops. Since it is not possible to develop the dislocation loops beyond the simulation box, we cannot grow the loops large enough to become visible as lines in the TEM images. For this reason, further development of the simulation approach and understanding of how large structures affect the dechanneling of ions is highly needed and further planned for future work.

Our results clearly show that the use of different probing beam energies provides additional and complementary information about the defect structures that is not accessible by single energy C-RBS measurements. For comparison, we have also simulated spectra using the structures where the damage was created by RDA. We can conclude that simulation of spectra by RDA does not give any additional information on defect type and does not follow the trend of the disorder with increase of the energy of the ion probing beam.

Finally, the main motivation for this work was to find out whether C-RBS spectra can give us the information about the nature of defects, with the help of simulations. This study is the first step of a broader goal to create a database of different defects in materials and how the different defects show up in C-RBS spectra. This would allow, on a longer times scale, to study the evolution of defects in situ by C-RBS, for example during annealing of the defects or during damage creation. With this first study we have shown that the necessary prerequisite for the main goal is the recoding of the C-RBS spectra with multiple-energy. Therefore, the information about the nature of the defects can only be obtained when the C-RBS spectra are recoded with multiple energies of the probing beam. The study also revealed the weaknesses of the MD modeling approach of limiting length scales which will be improved in the future.

## Declaration of Competing Interest

The authors declare that they have no known competing financial interests or personal relationships that could have appeared to influence the work reported in this paper.

## Acknowledgement

We would like to thank K. Hunger, J. Dorner and M. Fußeder from Max-Planck-Institut für Plasmaphysik for their technical support and Jintong Wu from the University of Helsinki for fruitful discussion.

This work has been carried out within the framework of the EUROfusion Consortium, funded by the European Union via the Euratom Research and Training Programme (Grant Agreement No 101052200 — EUROfusion). Views and opinions expressed are however those of the author(s) only and do not necessarily reflect those of the European Union or the European Commission. Neither the European Union nor the European Commission can be held responsible for them. M.L.C. acknowledges financial support from the research project “Captacion de Talento UAM” Ref: #541D300 supervised by the Vice-Chancellor of Research of Universidad Autonoma de Madrid (UAM). The authors acknowledge the support from the Slovenian Research Agency (research core funding No. P2–0405 and research project No. J2–3038). The authors wish to acknowledge CSC – IT Center for Science, Finland, for computational resources.

The authors acknowledge the support from The Centro de Microanalisis de Materiales (CMAM)-Universidad Autónoma de Madrid, for the beam time proposal (Multi-energy and multi-axial channeling study of induced damaged in W (111) crystals for DeHydroC project) with code STD039/22, and its technical staff for their contribution to the operation of the accelerator.

## Supplementary materials

Supplementary material associated with this article can be found, in the online version, at doi:10.1016/j.actamat.2023.119499.

## References

[1] O.V. Ogorodnikova, V. Gann, Simulation of neutron-induced damage in tungsten by irradiation with energetic self-ions, J. Nucl. Mater. 460 (2015) 60.
[2] B. Wielunska, M. Mayer, T. Schwarz-Selinger, A.E. Sand, W. Jacob, Deuterium retention in tungsten irradiated by different ions, Nucl. Fusion. 60 (2020), 096002.
[3] S. Das, H. Yu, E. Tarleton, F. Hofmann, The effect of helium implantation on the deformation behaviour of tungsten: X-ray micro-diffraction and nanoindentation, Sci. Rep. 9 (2019) 18354.
[4] Ł. Ciupiński, Ł. Ciupiński, O.V. Ogorodnikova, T. Płociński, M. Andrzejczuk, M. Rasiński, M. Mayer, K.J. Kurzydłowski, TEM observations of radiation damage in tungsten irradiated by 20 MeV W ions, Nucl. Instr. Method Phys. Res. Sect. B 317 (2013) 159–164, https://doi.org/10.1016/j.nimb.2013.03.022.
[5] J. Čižek, Characterization of lattice defects in metallic materials by positron annihilation spectroscopy: a review, J. Mater. Sci. Technol. 34 (2018) 577–598.
[6] J. Heikinheimo, K. Mizohata, J. Räisänen, T. Ahlgren, P. Jalkanen, A. Lahtinen, N. Catarino, E. Alves, F. Tuomisto, Direct observation of mono-vacancy and self-interstitial recovery in tungsten, APL Mater. 7 (2019), 021103, https://doi.org/10.1063/1.5082150.
[7] F. Tuomisto, I. Makkonen, Defect identification in semiconductors with positron annihilation: experiment and theory, Rev. Mod. Phys. 85 (2013) 1583–1631.
[8] Z. Hu, P. Desgardin, C. Genevois, J. Joseph, B. Décamps, R. Schäublin, M.-F. Barthe, Effect of purity on the vacancy defects induced in self–irradiated tungsten: a combination of PAS and TEM, J. Nucl. Mater. 556 (2021) 153175, https://doi.org/10.1016/j.jnucmat.2021.153175.
[9] S. Wang, W. Guo, T. Schwarz-Selinger, Y. Yuan, L. Ge, L. Cheng, X. Zhang, X. Cao, E. Fu, G.-H. Lu, Dynamic equilibrium of displacement damage defects in heavy-ion irradiated tungsten, Acta Mater. 244 (2023) 118578, https://doi.org/10.1016/j.actamat.2022.118578.
[10] W. Jiang, Y. Zhu, L. Zhang, D.J. Edwards, N.R. Overman, G. Nandipati, W. Setyawan, C.H. Henager, R.J. Kurtz, Dose rate effects on damage accumulation and void growth in self-ion irradiated tungsten, J. Nucl. Mater. 550 (2021) 152905, https://doi.org/10.1016/j.jnucmat.2021.152905.
[11] A. Vantomme, 50years of ion channeling in materials science, Nucl. Instr. Methods Phys. Res. Sect. B 371 (2016) 12–26, https://doi.org/10.1016/j.nimb.2015.11.035.

[12] L.C. Feldman, J.W. Mayer, S.T. Picraux. Materials analysis by ion beam channeling, Academic Press, New York, 1982.
[13] W.-K. Chu, J.W. Mayer, M. Nicolet, Backscatering Spectrometry, Academic Press, San Diego, 1978.
[14] S. Zhang, K. Nordlund, F. Djurabekova, Y. Zhang, G. Velisa, T.S. Wang, Simulation of Rutherford backscattering spectrometry from arbitrary atom structures, Phys. Rev. E 94 (2016), https://doi.org/10.1103/PhysRevE.94.043319.
[15] P. Jozwik, L. Nowicki, R. Ratajczak, A. Stonert, C. Mieszczynski, A. Turos, K. Morawiec, K. Lorenz, E. Alves, Monte Carlo simulations of ion channeling in crystals containing dislocations and randomly displaced atoms, J. Appl. Phys. 126 (2019) 195107, https://doi.org/10.1063/1.5111619.
[16] S. Zhang, K. Nordlund, F. Djurabekova, F. Granberg, Y. Zhang, T.S. Wang, Radiation damage buildup by athermal defect reactions in nickel and concentrated nickel alloys, Mater. Res. Lett. 5 (2017) 433–439, https://doi.org/10.1080/21663831.2017.1311284.
[17] Y. Zhou, G. Velişa, S. San, M.L. Crespillo, Z. Fan, H. Bei, W.J. Weber, P. Xiu, L. Wang, F. Tuomisto, W.-Y. Ching, Y. Zhang, Role of chemical disorder on radiation-induced defect production and damage evolution in NiFeCoCr, J. Nucl. Mater. 565 (2022) 153689, https://doi.org/10.1016/j.jnucmat.2022.153689.
[18] K. Nordlund, F. Djurabekova, G. Hobler, Large fraction of crystal directions leads to ion channeling, Phys. Rev. B 94 (2016), 214109.
[19] T. Schwarz-Selinger, Deuterium retention in MeV self-implanted tungsten: influence of damaging dose rate, Nucl. Energy Mater. 12 (2017) 683–688.
[20] B. Wielunska, T. Płociński, T. Schwarz-Selinger, M. Mayer, W. Jacob, L. Ciupiński, Dislocation structure of tungsten irradiated by medium to high-mass ions, Nucl. Fusion 62 (2022), 096003, https://doi.org/10.1088/1741-4326/ac75ff.
[21] ASTM Int'l E521-16, Standard practice for neutron radiation damage simulation by charge-particle irradiation. Annual Book of ASTM Standards vol 12.02, American Society for Testing and Materials, Philadelphia, PA, 2016, p. 8.
[22] J.F. Ziegler, J.P. Ziegler, M.D. Biersack, SRIM - The Stopping and Range of Ions Ion Matter, SRIM, Chester, Maryland, USA, 2008.
[23] A. Redondo-Cubero, M.J.G. Borge, N. Gordillo, P.C. Gutiérrez, J. Olivares, R. Pérez Casero, M.D. Ynsa, Current status and future developments of the ion beam facility at the centre of micro-analysis of materials in Madrid, Eur. Phys. J. Plus 136 (2021) 175, https://doi.org/10.1140/epjp/s13360-021-01085-9.
[24] A. Šestan, P. Jenuš, S.N. Krmpotič, J. Zavašnik, M. Čeh, The role of tungsten phases formation during tungsten metal powder consolidation by FAST: implications for high-temperature applications, Mater. Charact. 138 (2018) 308–314, https://doi.org/10.1016/j.matchar.2018.02.022.
[25] X. Jin, J.-P. Crocombette, F. Djurabekova, S. Zhang, K. Nordlund, F. Garrido, A. Debelle, New developments in the simulation of Rutherford backscattering spectrometry in channeling mode using arbitrary atom structures, Modell. Simul. Mater. Sci. Eng. 28 (2020), 075005, https://doi.org/10.1088/1361-651X/ab81a9.
[26] M. Ghaly, K. Nordlund, R.S. Averback, Molecular dynamics investigations of surface damage produced by kiloelectronvolt self-bombardment of solids, Philos. Mag. A 79 (1999) 795–820, https://doi.org/10.1080/01418619908210332.
[27] K. Nordlund, Molecular dynamics simulation of ion ranges in the 1–100 keV energy range, Comput. Mater. Sci. 3 (1995) 448–456, https://doi.org/10.1016/0927-0256(94)00085-Q.
[28] K. Nordlund, M. Ghaly, R.S. Averback, M. Caturla, T. Diaz de la Rubia, J. Tarus, Defect production in collision cascades in elemental semiconductors and fcc metals, Phys. Rev. B 57 (1998) 7556–7570, https://doi.org/10.1103/PhysRevB.57.7556.
[29] F. Granberg, J. Byggmästar, K. Nordlund, Molecular dynamics simulations of high-dose damage production and defect evolution in tungsten, J. Nucl. Mater. 556 (2021), 153158.
[30] M.J. Norgett, M.T. Robinson, I.M. Torrens, A proposed method of calculating displacement dose rates, Nucl. Eng. Des. 33 (1975) 50–54.
[31] S.F. Plimpton, Fast parallel algorithms for short-range molecular dynamics, J. Comput. Phys 117 (1995) 1–19.
[32] A.P. Thompson, H.M. Aktulga, R. Berger, D.S. Bolintineanu, W.M. Brown, P. S. Crozier, P.J. in 't Veld, A. Kohlmeyer, S.G. Moore, T.D. Nguyen, R. Shan, M. J. Stevens, J. Tranchida, C. Trott, S.J. Plimpton, LAMMPS - a flexible simulation tool for particle-based materials modeling at the atomic, meso, and continuum scales, Comput. Phys. Commun. 271 (2022) 108171, https://doi.org/10.1016/j.cpc.2021.108171.
[33] G.J. Ackland, R. Thetford, An improved N-body semi-empirical model for body-centred cubic transition metals, Philos. Mag. A 56 (1987) 15–30.
[34] Y. Zhong, K. Nordlund, M. Ghaly, R.S. Averback, Defect production in tungsten: a comparison between field-ion microscopy and molecular-dynamics simulations, Phys. Rev. B 58 (1998) 2361–2364.
[35] S. Hasanzadeh, R. Schäublin, B. Décamps, V. Rousson, E. Autissier, M.F. Barthe, C. Hébert, Three-dimensional scanning transmission electron microscopy of dislocation loops in tungsten, Micron 113 (2018) 24–33, https://doi.org/10.1016/j.micron.2018.05.010.
[36] U.M.U. Martin, H. Oettel, The quantitative measurement of dislocation density in the transmission electron microscope, Prakt. Metallogr. 32 (9) (1995) 467–476.
[37] T. Kruml, V. Paidar, J.L. Martin, Dislocation density in Ni3(Al,Hf), Intermetallics 8 (2000) 729–736.
[38] K. Jin, G. Velisa, H. Xue, T. Yang, H. Bei, W.J. Weber, L. Wang, Y. Zhang, Channeling analysis in studying ion irradiation damage in materials containing various types of defects, J. Nucl. Mater. 517 (2019) 9–16, https://doi.org/10.1016/j.jnucmat.2019.01.033.
[39] M.J. Banisalman, S. Park, T. Oda, Evaluation of the threshold displacement energy in tungsten by molecular dynamics calculations, J. Nucl. Mater. 495 (2017) 277–284.
[40] A. Stukowski, V.V. Bulatov, A. Arsenlis, Automated identification and indexing of dislocations in crystal interfaces, Model. Simul. Mater. Sci. Eng. 20 (2012), 085007, https://doi.org/10.1088/0965-0393/20/8/085007.
[41] Babel, "http://emmanuel.clouet.free.fr/Programs/Babel/," [Online].
[42] Y. Quéré, About the dechanneling due to dislocation loops, Radiat. Eff. 38 (1978) 131.
[43] A. Reza, H. Yu, K. Mizohata, F. Hofmann, Thermal diffusivity degradation and point defect density in self-ion implanted tungsten, Acta Mater. 193 (2020) 270–279.
[44] D.R. Mason, F. Granberg, M. Boleininger, T. Schwarz-Selinger, K. Nordlund, S. L. Dudarev, Parameter-free quantitative simulation of high-dose microstructure and hydrogen retention in ion-irradiated tungsten, Phys. Rev. Mater. 5 (2021) 095403, https://doi.org/10.1103/PhysRevMaterials.5.095403.